# PCCP

## Accepted Manuscript

# Nanoalloy Electrocatalysis: Simulating Cyclic Voltammetry from Configurational Thermodynamics with Adsorbates

*Lin-Lin Wang[1*], Teck L. Tan[2] and Duane D. Johnson[1,3§]*

[1]Ames Laboratory, U.S. Department of Energy at Iowa State University, Ames, IA 50011, USA

[2]Institute of High Performance Computing, Agency for Science, Technology and Research, Singapore 138632, Singapore

[3]Department of Materials Science and Engineering, Iowa State University, Ames, IA 50011, USA

ABSTRACT: We simulate the adsorption isotherms for alloyed nanoparticles (nanoalloys) with adsorbates to determine cyclic voltammetry (CV) during electrocatalysis. The effect of alloying on nanoparticle adsorption isotherms is provided by a hybrid-ensemble Monte Carlo (MC) simulation that uses the cluster expansion method extended to non-exchangeable coupled lattices for nanoalloys with adsorbates. Exemplified here for the hydrogen evolution reaction, a 2-dimensional CV is mapped for Pd-Pt nanoalloys as a function of both electrochemical potential and the global Pt composition, and shows a highly non-linear alloying effect on CV. Detailed features in CV arise from the interplay among the multi-site H-adsorption that closely correlated to alloy configurations, which are in turn affected by the H-coverage. The origins of specific features in CV curves are assigned. The method provides a more complete means to design nanoalloys for electrocatalysis.

1

For nanoalloys, such as transition-metal alloyed nanoparticles (NPs) used as heterogeneous catalysts, besides structural motifs[1], *alloy configuration* or *chemical order* can be altered by their operational chemical environment.[2-5] It has been shown that the enhanced catalytic functionality of nanoalloy catalysts highly depends on the configurational thermodynamics, or distribution of atoms on different sites.[6-9] Although certain core-shell configurations with different degree of mixing in alloyed NPs can be synthesized, the thermodynamic stability of such configurations is often an open question. Thus, an accurate description of the configurational thermodynamics of alloyed NPs, especially under chemical working conditions, is crucial to understand their functionality and stability for the design of new nanoalloy catalysts.[10]

For alloyed NPs, the exponential number of alloy configurations with many different types of low-coordinated sites makes theoretical studies on configurational thermodynamic challenging. Cluster expansion[11] (CE) method coupled with density functional theory[12,13] (DFT) calculations and Monte Carlo (MC) simulations, proven enormously successful for bulk alloys[14-23] and surfaces[24,25], have been extended to study the configurational thermodynamics of alloyed NPs *without* adsorbates[26-31] beyond core-shell preferences[32]. More recently, by extending the CE formalism of a non-exchangeable coupled-lattice[33] to alloyed NPs with adsorbates[10], we have treated substrate-adsorbate and adsorbate-adsorbate interactions on an equal footing with substrate-substrate interactions to study the configurational thermodynamics in alloyed NPs and the changes induced by adsorbates, including reversal of core-shell preference.

Here we focus on the NP alloying effect on adsorption isotherm and determine the cyclic voltammetry (CV) in electrocatalysis.[34-36] To simulate adsorption isotherm on the non-exchangeable coupled-lattice in MC simulation, we propose a hybrid ensemble scheme, where the alloy substrate and adsorbates take MC steps within the canonical and grand canonical

ensemble, respectively. Using the optimal CE fitted to DFT calculations, we simulate the H-adsorption isotherm on alloyed PdPt NPs to calculate the CV for the hydrogen evolution reaction (HER) with the NP alloying effect on H-adsorption included.

Pd-Pt nanoalloys with varying size, shape, and composition have been found to offer enhanced electrocatalytic activity for methanol oxidation[37], oxygen reduction[38], formic acid oxidation[39] and $H_2O_2$ reduction[40]. Previously, we have searched for ground-state (GS) configurations of PdPt alloyed NPs to study H-adsorption and design electrocatalysts for HER at low H-coverage.[28] At medium to high H-coverages, the effect of adsorbate-adsorbate interactions becomes important, and so are the adsorbate-induced nanoalloy configurational changes, which can affect the adsorption isotherm. All these features can now be treated in the non-exchangeable coupled-lattice CE as proposed for alloyed NPs with adsorbates.[10]

We find that the Pt-core/Pd-shell preference is reversed at high H-coverage. By decomposing the adsorption isotherm and the associated CV to site contributions and mapping the 2D CV as a function of both electrochemical potential (U) and the overall Pt composition ($c_{Pt}$), we find that the alloying effect proceed in a highly non-linear manner. The evolution of the features in CV correlates closely with the nanoalloy configurations, which in turn is affected by the H-coverage. Our MC simulations with the hybrid ensemble scheme based on the non-exchangeable coupled-lattice CE can quantitatively describe the coupling of nanoalloy configuration to the adsorption isotherm to achieve design of nanoalloy electrocatalysts under working conditions.

**Computational Methods.** Non-exchangeable coupled-lattice CE has enabled the study of the configurational thermodynamics of nanoalloys in a chemical reactive environment.[10] MC simulations can be used to extract the adsorption isotherm of adsorbate-covered surfaces[41] and NPs, with its derivative used to calculate CV.[34-36]

HER is divided into steps: $H^+ + e^- \rightarrow H^*$ (Volmer) followed by either $H^* + H^* \rightarrow H_2(g)$ (Tafel) or $H^* + H^+ + e^- \rightarrow H_2(g)$ (Heyrovsky). For Pt catalysts, the Volmer step is in quasi-equilibrium due to the much lower kinetic barrier than the other two steps, either of which can be the rate-limiting step. Following the kinetic analysis by Norskov *et al.*[42], by taking the standard hydrogen electrode (SHE) with $H_2$ at 1 *atm* and *pH*=0 for the solution at room temperature, the reaction barrier can be approximated by the free-energy change for the intermediate state H*.

A MC simulation using an optimal CE can be used to compute the H-adsorption isotherms for the Volmer step at equilibrium under an electrochemical potential U.[34] For nanoalloys, the result is the equilibrium H-coverage, $\theta$, as a function of both U and composition, i.e., $c_{Pt}$ for Pd-Pt. The theoretical maximum limit of the exchange current is obtained via $d\theta/dU$ as in

$j_{max} = \pm \dfrac{dQ}{dt} = \pm \dfrac{dQ}{d\theta}\dfrac{d\theta}{dU}\dfrac{dU}{dt}$. Here, $Q = Q_o\theta$ and $Q_o$ is the charge per unit area converted for 1 monolayer (ML) of H-coverage. Hence, $dQ/d\theta$ is a constant and has about the same value for Pt and Pd NP (because they have similar inter-atomic distance); $dU/dt$ is the sweeping rate, which can be regarded as a constant. So, the peak positions in CV as a function of U is determined by the derivative of the H-adsorption isotherm, i.e., $d\theta/dU$.

In CE[11], any physical quantity as a function of configurational variables on fixed lattices can be expanded in the basis of a series of cluster correlation functions.[43] Here, for a system with two coupled lattices of non-exchangeable configurations, we expand the formation energy as,

$$E(\sigma,\delta) = \sum_{\alpha\beta} V_{\alpha\beta}\Theta_{\alpha\beta}(\sigma,\delta) = \sum_{\alpha\beta} V_{\alpha\beta}\Phi_\alpha(\sigma)\Psi_\beta(\delta)$$
$$= V_0 + (\sum_i V_i^S \sigma_i + \sum_{i,j} V_{ij}^S \sigma_i\sigma_j + \cdots) + (\sum_i V_i^A \delta_i + \sum_{i,j} V_{ij}^A \delta_i\delta_j + \cdots) + (\sum_{i,j} V_{ij}^C \sigma_i\delta_j + \cdots)$$

(1)

where $\Theta_{\alpha\beta}(\sigma,\delta) = \Phi_\alpha(\sigma)\Psi_\beta(\delta)$ are the products of cluster correlation functions on two coupled lattices and $V_{\alpha\beta}$ are the corresponding effective cluster interactions (ECIs) to be determined via

4

structural inversion and cluster selection.[44] Because the orthogonality of primitive basis functions is always preserved in the construction of high-dimensional vector space by outer (tensor) products, a coupled lattice with non-exchanging species that works for ionic systems[33] will also work for adsorbates on alloyed surfaces[45,46] and NPs. The second line is explicitly for a binary alloy substrate with one type of adsorbate, using site-occupation variables, $\sigma_i$ or $\delta_i$, which equal 1 (0) if site $i$ is occupied (not occupied). The ECIs for substrate, adsorbate and coupled clusters are denoted with superscript S, A, and C, respectively. As extended here, the CE enables coverage-dependent studies on the thermodynamics of alloyed NPs and surfaces with adsorbates.

The formation energy per site ($E_f$) for the PdPt NPs with H-coverage is defined as

$$E_f = \frac{1}{(N_S + N_A)} \left[ E_{tot} - n_{Pt}E_{Pt} - (N_S - n_{Pt})E_{Pd} - \frac{1}{2}n_H E_{H_2} \right], \tag{2}$$

which is calculated from the DFT total energies of the system ($E_{tot}$) referenced to NPs of pure Pd ($E_{Pd}$) and Pt ($E_{Pt}$) along with $H_2$ molecule ($E_{H_2}$). The number of substrate sites, adsorbate sites, Pt atoms, and H atoms are denoted by $N_S$, $N_A$, $n_{Pt}$ and $n_H$, respectively. We also define the overall Pt composition as $c_{Pt} = n_{Pt}/N_S$, the shell concentration of Pt as $c_{Pt}^{shell} = n_{Pt}^{shell}/N_S^{shell}$ and H-coverage as $\theta = n_H / N_S^{shell}$, where $N_S^{shell}$ is the number of shell sites in the substrate.

Figure 1 shows the non-exchangeable coupled-lattices for H-adsorption on a cuboctahedral NP ($N_S = 55$, $N_A = 122$ and $N_S^{shell} = 42$). The $O_h$ symmetry greatly reduces the number of symmetry unique types of site (or 1-body ECIs). As shown in Fig. 1(a) and (b), there are five and six types in the substrate and adsorbate lattices, respectively. An fcc-bridge (brf) site is on the edge of the NP, which can be viewed as bridge (brg) or fcc site for {100} or {111} facet, respectively. The 4-fold hollow site on {100} facet is not included because H-adsorption on this

5

site is unlikely: (i) its binding strength is much weaker than the neighboring brf site and (ii) once

the brf sites are occupied, it is highly unfavorable to occupy the 4-fold hollow site as the distance

between them is very short, implying strong H-H repulsion. For similar reasons, we exclude hcp

site on {111} facet in favor of the neighboring fcc and brf sites. Unlike O-adsorption on PdRh

NPs[10], we also consider three different types of atop H-adsorption sites (Fig.1), each for every

substrate site on the shell; because two population of H*, one strongly and the other weakly

bonded are present.[47,48] So the highest coverage is 122 H atoms or 2.9 ML. From a pool of 11 1-

body, 85 2-body, 168 3-body and 16 4-body clusters, an optimally truncated CE is selected via

the leave-one-out cross-validation (CV-1).



(a)                                      (b)
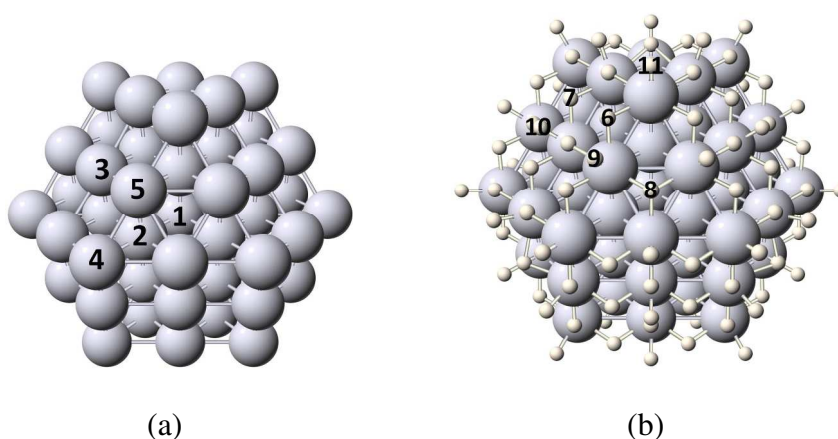
**Figure 1.** For a 55-atom cuboctahedral NP with 122 adsorption sites, the CE distinctive 1-body

or $O_h$ symmetry *inequivalent* sites in the (a) substrate and (b) adsorbate sublattices.   The

substrate sites are composed of *five* types: 1 central-core (ccr), 12 second-core (scr), 6 {100}-

center (sqr), 12 corner (crn) and 24 edge (edg) sites. The adsorbate lattice has *six* different types:

48 bridge-fcc (brf), 24 bridge (brg), 8 fcc, 24 top-edge (ted), 6 top-{100}-center (tsq) and 12 top-

corner (tcn) sites. Eleven inequivalent sites are numbered: ccr (1), scr (2), sqr (3), crn (4) and edg

(5) substrate site, and brf (6), brg (7), fcc (8), ted (9), tsq(10) and tcn (11) adsorption site.

We search for GS configurations and optimize CE simultaneously via an iterative approach by thermal annealing within the MC simulation followed by DFT verification round-by-round. Although a heterogeneous system, we find that Pd-Pt interaction and metal-H interaction have comparable strength. So the two-step approach[10] developed for systems with largely different interactions, such as Pd-Pt-O, is unnecessary here. For the Pd-Pt-H system, fitting CE in one-step is enough to achieve small prediction errors and fast convergence to the GSs.

For DFT calculations, we use a cubic cell of 19.2 Å enclosing the cuboctahedral NP, ensuring sufficient vacuum. DFT calculations used the revised PBE exchange-correlation functional[49], and a plane-wave basis-set within the projected-augmented-wave method, as implemented in the *Vienna Ab initio Simulation Package* (VASP)[50,51]. A kinetic energy cutoff of 400 eV and $\Gamma$-point with a Gaussian smearing of 0.05 eV were used to calculate total energies (converged to 2 $m$eV/atom) and relax structures (magnitude of force per atom below 0.1 eV/Å). For the thermal annealing in MC simulation, we start from 2784 K, using a step size of 116 K until it reaches 116 K with $5 \times 10^3$ sampling MC steps at each temperature. For the configurational thermodynamics to simulate H-adsorption isotherm at 298 K, we use $1 \times 10^5$ sampling MC steps.

To sample the low-energy configurations of the nanoalloy with adsorbate efficiently for adsorption isotherm, we propose a hybrid ensemble scheme during MC simulation, where the substrate takes canonical steps to change alloy configuration with $n_{Pt}$ fixed and the adsorbate takes grand canonical steps to allow both $n_H$ and adsorbate configurations to change. This scheme can be justified as follows: In an electrochemical setting, the chemical potential of the adsorbate is tuned continuously by sweeping U to achieve equilibrium between adsorbate and ions in solution, as in a grand canonical ensemble. In contrast to the reservoir of adsorbates in the

surrounding environment, the NP catalyst embedded in the electrode after synthesis has no such reservoir of Pd and Pt atoms in an electrochemical cell, and is thus suitable for canonical ensemble. We reasonably assume that leaching and sintering of NP catalysts are much slower processes than H-adsorption, desorption and intra-NP diffusion during HER. For nanoalloys with adsorbates, we sample the system's formation energy as a function of both adsorbate and alloy configurations. All the energy changes fitted in CE and sampled in MC are in reference to pure metal NPs and free adsorbate molecules; this avoids the calculation of adsorption energy, which depends on the choice of the different alloy configurations.

**Results and Discussion.** *Nanoalloy Stability and Groundstates.* For Pd-Pt-H NPs, after five rounds of CE fitting using a thermal-annealing GS search with DFT verification, no new GSs are found. The CV-1 score is 0.89 $m$eV. Figure 2 shows the GS hull versus $n_{Pt}$ at selected H-coverages ($n_H = 20$, 40, 60, 80 and 100) for CE fitting, and one ($n_H = 50$) for validation. Representative GS configurations are presented in Fig. 3 to show the site preferences. The mean absolute error in predicting new structural energies decreases round by round and reaches 2.2 $m$eV after five rounds. During the construction of the optimal CE and GS search, 2133 structural energies have been calculated in DFT.

At zero H-coverage ($n_H = 0$), as we have previously studied[28], PdPt NP has a strong Pt-core/Pd-shell preference. With increasing $n_{Pt}$, Pt first occupies the central-core (ccr) site followed by the second-core (scr) sites to form the core-shell NP at $Pd_{42}Pt_{13}$. As $n_{Pt}$ increases further, Pt starts to occupy the edge (edg), {100}-center (sqr) and corner (crn) site in the shell.

At $n_H = 20$ (Fig. 2(a) and Fig. 3(a)), a single Pt atom prefers the edge site in the shell (as opposed to the central-core site at $n_H = 0$) and binds to two H at the brf sites; the other H atoms

8

bind to Pd atom at brf sites. As $n_{Pt}$ increases, more Pt stays in the shell to bind with H till

$n_{Pt} = 7$ in $Pd_{48}Pt_7H_{20}$, when Pt starts to occupy the central-core and then second-core sites. In

$Pd_{31}Pt_{24}H_{20}$, core sites are fully occupied by Pt, while Pt-H at brf sites in the shell persists. Upon

further increase in composition, extra Pt occupies the shell again and H at brg sites on {100}

facets also appear as in Pt-rich $Pd_7Pt_{48}H_{20}$. The formation energy $E_f$ starts at −0.040 eV/atom for

$Pd_{55}H_{20}$, and reaches −0.078 eV/atom for $Pd_{31}Pt_{24}H_{20}$ at the bottom of the GS hull.

At $n_H = 40$ (Fig. 2(b) and Fig. 3(b)) with higher H-coverage, the Pt at the edge site on the

shell can bind to 4 H atoms, two brf, one brg and one fcc. As more Pt appears in the shell, Pt at

the corner site also binds to 4 H atoms, all brf. As $n_{Pt}$ increases, more Pt first stay at the edge

and corner sites in the shell, then go into the core as in $Pd_{43}Pt_{12}H_{40}$, until the whole core region is

filled with Pt as in $Pd_{18}Pt_{37}H_{40}$. Notably Pt does not favor sqr site on {100} facet. As in

$Pd_6Pt_{49}H_{40}$, all six sqr sites are occupied by Pd without H-binding, which points to that the Pt-H

interaction is stronger than Pd-H, especially for {100} facet.

At $n_H = 50$, whose DFT energies are not included into the training dataset for CE, the

convergence of the GSs in Fig. 2(c) is a proof that our optimal ECIs fitted from the selected H-

coverages are also good for other H-coverages. The behavior in site occupation is similar to

$n_H = 40$. For Pt at the corner site on the shell, it can bind to 5 H atom, including one tcn-H.

Compared to $Pd_{18}Pt_{37}H_{40}$ with just one less Pt, $Pd_{19}Pt_{36}H_{50}$ has now several second-core sites

occupied by Pd, demonstrating that an increasing H-coverage tends to reverse the NP's core-

shell preference. Again, Pt avoids sqr site and they are all occupied by Pd, as in $Pd_6Pt_{49}H_{50}$.
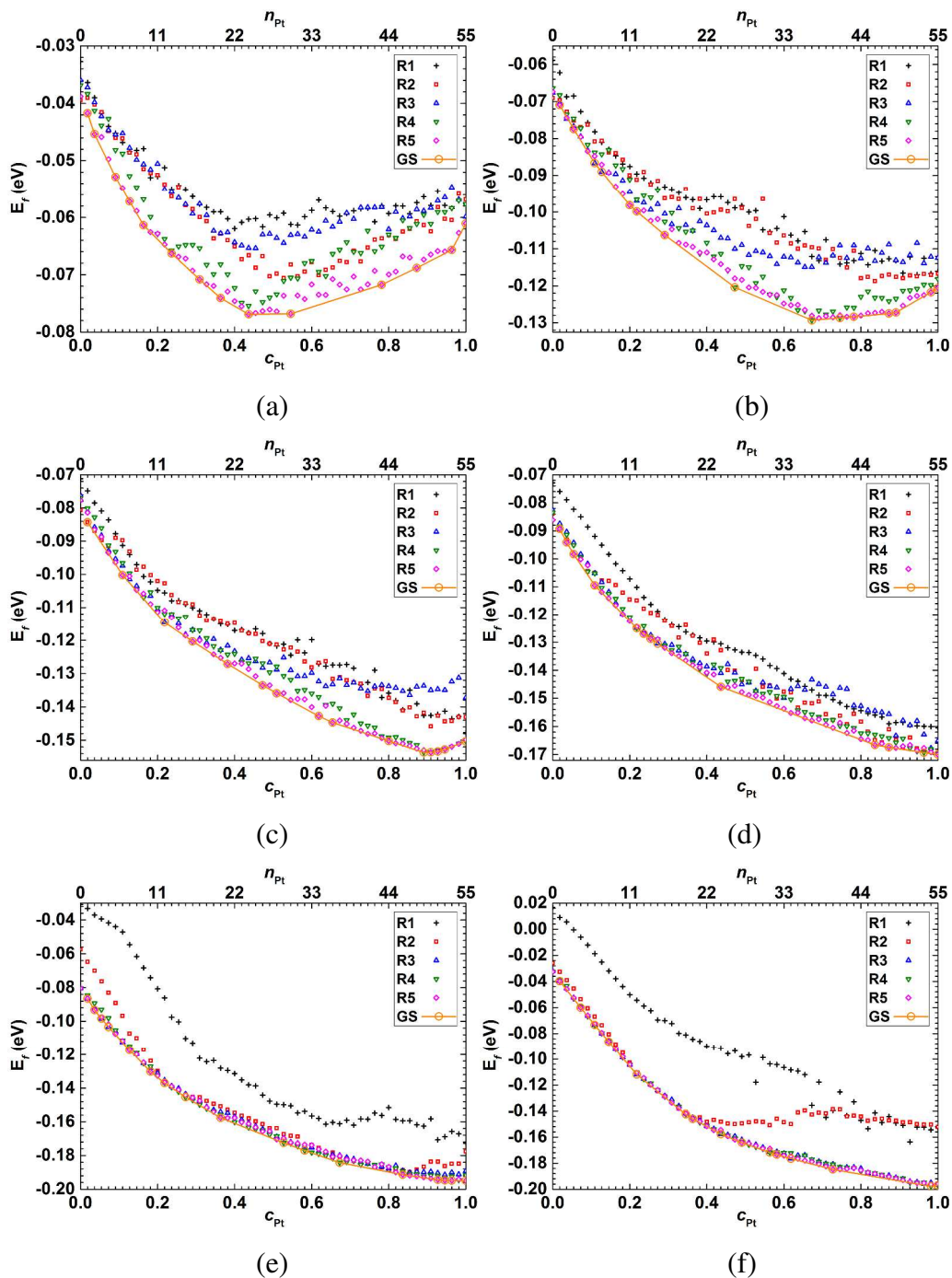
**Figure 2.** Ground-state (GS) hull with DFT-evaluated $E_f$ as a function of $c_{Pt}$ for H-coverages of (a) 20, (b) 40, (c) 50, (d) 60, (e) 80 and (f) 100. R1 to R5 refers to predicted GS configurations from each of the five rounds of CE plus thermal annealing. Selected GSs are shown in Fig.3.
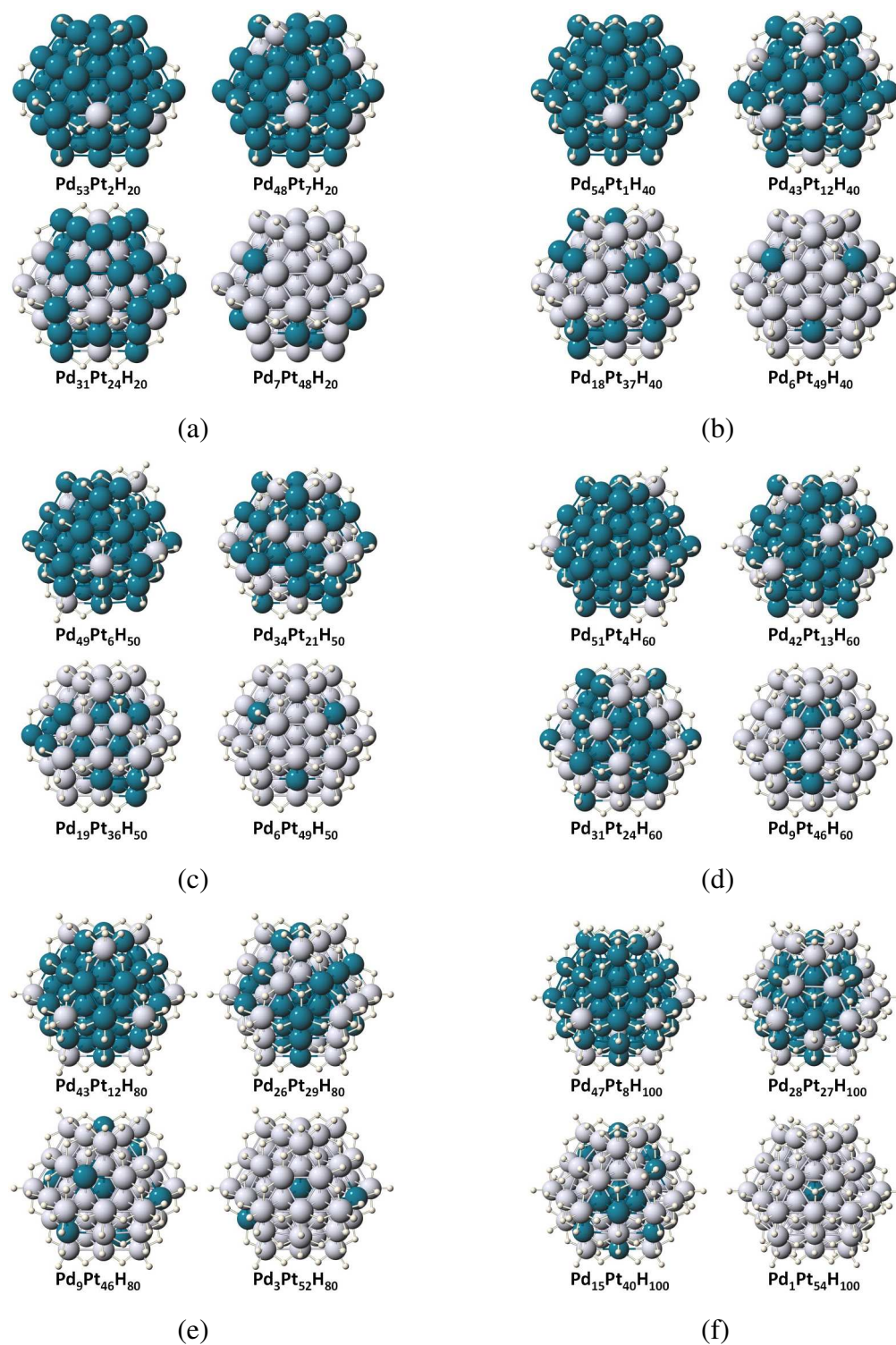
**Figure 3.** Selected configurations on the GS hull (Fig. 2) for H-coverages of (a) 20, (b) 40, (c) 50, (d) 60, (e) 80 and (f) 100. Pd, Pt, and H are denoted by blue, gray and small white spheres, respectively.

11

At $n_H = 60$ (Fig. 2(d) and Fig. 3(d)), with higher H-coverage, the Pt of Pt-poor NPs on the shell now prefers corner site to bind to 5 H atoms instead of the edge site with 4 H as in $Pd_{51}Pt_4H_{60}$. For $n_{Pt} = 24$, all Pt occupy shell sites in binding to H and the core site are all Pd. Only at higher $n_{Pt}$, the central-core site becomes Pt as in $Pd_9Pt_{46}H_{60}$.

At $n_H = 80$ (Fig. 2(e) and Fig. 3(e)), the corner-Pt binds to 5 H and becomes more favored – because all 12 corners in $Pd_{43}Pt_{12}H_{80}$ now have this feature and tcn-H persists as Pt content increases. The central-core site is now almost exclusively occupied by Pd. At $n_H = 100$ (Fig. 2(f) and Fig. 3(f)), as the H-coverage approaches the highest limit, other atop sites for H become occupied besides all other H sites are fully occupied. The short distance among H atoms cause repulsion, as the formation energy does not go any lower when comparing Fig. 2(f) to (e). The last Pd replaced by Pt is the central-core site, in distinct contrast to pure PdPt NP. But the 13-atom core region is not full of Pd at the Pt-rich end as in $Pd_{15}Pt_{40}H_{100}$ with such high H-coverage. This outcome deviates from the simple core-shell reversal picture found in PdRhO NPs, where Rh-O interaction is much stronger than Pd-O.[10]

*Effective Cluster Interactions.* We plot the ECIs from the optimal CE in Fig. 4. Among the eleven 1-body ECIs, the first five are for substrate sites. The ECIs for central-core and second-core sites are negative, with the central-core being the most favorable for Pt. The 1-body ECIs for the shells sites are also negative except for the corner site. The first pair ECIs among substrate sites are mostly positive, favoring alloy. So without H, the PdPt NPs have a preference for Pt-core and Pd-shell (but not as strong as Pd-Rh). The other six 1-body ECIs are for the adsorbate sites, with three of them negative (brf, brg and fcc) and two are slightly positive (ted and tsq) and one large positive (tcn). So for Pd-H interaction, atop H-adsorption is not favorable.

12

The magnitudes of the 1-body adsorbate ECIs are comparable to those for substrate sites, in contrast to PdRhO system, where metal-O ECIs are much stronger than metal-metal ones.[10]
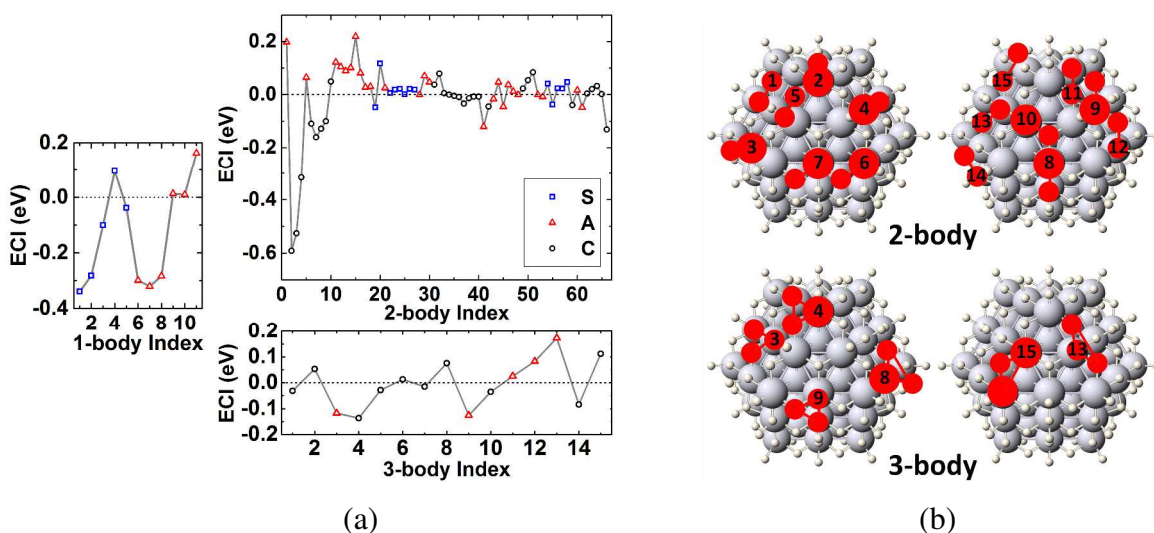


**Figure 4.** Optimized ECIs of (a) 1-, 2- and 3-body with selected ones shown in (b). ECIs among substrate (S), adsorbate (A) and the coupled (C) are indicated in blue squares, red triangles and black circles, respectively. Indices for 1-body ECIs are illustrated in Fig. 1.

Among the 2-body ECIs shown in Fig. 4(a), the first pair ECIs for the coupled interactions between metal and H are dominant, all negative and the magnitude is even larger than metal-metal ECIs. This means that the Pt-H interactions are stronger than Pd-H. The first three coupled ECIs (indices 2, 3 and 4) between shell sites and their atop adsorption sites are largely negative, pointing favorability of atop H-adsorption on Pt, in distinct contrast to Pd. The next four coupled ECIs (indices 6, 7, 8 and 9) between shell sites with non-atop adsorption sites are also negative, which gives stronger Pt-H interactions than Pd-H in general. The ECIs between adsorbate sites of short distances are all positive, showing the repulsion among adsorbed H. The 3-body coupled ECIs also have sizable magnitude, showing the delicacy of all three types of interactions. These features of the ECIs can explain the trends of GS configurations in Fig. 2 and 3.

13

***Monte Carlo Simulations with Hybrid Ensemble for Cyclic Voltammetry.*** Using the hybrid sampling ensemble suitable for alloyed NP with adsorbates, we simulate the H-adsorption isotherm $\theta(U, c_{Pt})$ at 298 K by varying the chemical potential of H for a fixed Pt composition in each MC run. We plot in Fig. 5 the derivative of $\theta(U)$ and its decomposition to different adsorption sites for $Pd_{55}$, $Pt_{55}$ and $Pd_{36}Pt_{19}$ in (a), (b) and (c), respectively. The results show the NP alloying effect on CV (free energy difference due to translational, rotational and vibrational contributions of $H_2$ vs. H* are included, and give an approximately uniform shift of 0.2 V in U).

For pure Pd, the decomposed CV peaks can be divided into two groups: low and high U. At high-U range for strongly-bonded H, the group includes fcc-H with one peak, brf-H with two peaks and brg-H with three peaks. The splitting of brf-H and brg-H is caused by the interplay of multi-site adsorption. As U is swept from high to low, H* first appears simultaneously on brf, brg and fcc sites, because their 1-body ECIs are almost equal (Fig. 4(a) 1-body indices 6, 7 and 8). The higher peak for brf than brg and fcc is due to the larger number of brf sites. When more brf sites are occupied by H on all the edges of Pd NP, because of the repulsive 2-body ECIs between H* (Fig. 4(a) 2-body indices 1, 5 and 11-15), they repel mostly the nearest-neighbor brg-H and to a lesser amount the fcc-H further away. This repulsion effect slows down the occupation of brg site and causes a split in brg-H peak (one at ~0.2 V and one at 0.05 V). As U goes below 0, H-coverage gets higher and the repulsion between brf-H and brg-H becomes stronger and cause further splitting for each of them into two peaks. As a result, contributions from three different sites (brf, brg and fcc) overlap and sum up to the first overall peak at U = 0.2 V. As U becomes more negative and at very high H-coverage, the three atop-H sites (ted, tsq and tcn) become occupied; whose peak positions reflect the collective effect of single and multi-body ECIs.

14
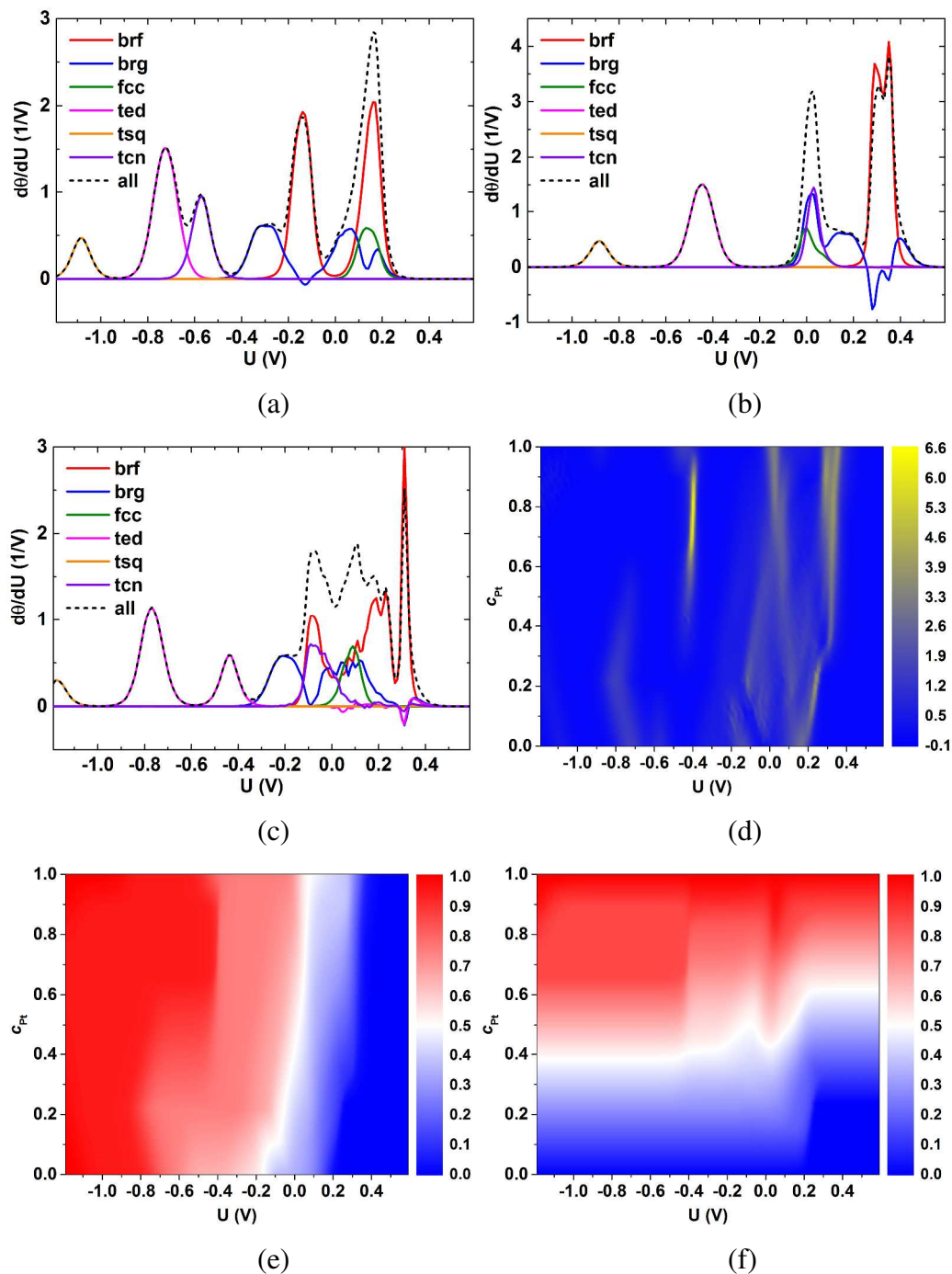
**Figure 5.** From hybrid-ensemble MC simulations at 298 K, CV (d$\theta$/dU) for HER on (a) Pd$_{55}$, (b) Pt$_{55}$ and (c) Pd$_{36}$Pt$_{19}$ NPs with decomposition to six adsorption sites (Fig. 1). 2D color contours of (d) CV, (e) H-coverage $\theta$, and (f) shell concentration $c_{Pt}^{shell}$ as functions of both U and $c_{Pt}$. Plots (a), (b), and (c) are simply a "line cut" through (d) at $c_{Pt}$ = 0, 1, and 0.35, respectively.

In contrast to pure Pd, the three atop-H sites for pure Pt NP are more favored than Pd, as shown by the strong negative 2-body ECIs (Fig. 4(a) 2-body indices 2, 3 and 4), which corresponds to the shift of the three peaks to higher U than for Pd, particularly the tcn-H. On the other hand, the fcc-H on Pt is not as strongly bonded as on Pd, so the fcc-H peak is shifted towards lower U and even lower than tcn-H. Also, at high-U range, brg-H site is a little more preferred than brf-H on Pt. As U is swept from high to low, H* first appears on brg then followed closely by brf sites at ~0.35 V. However, due to the strong repulsion between them, H occupation on brf will deplete those on brg sites and give two negative but connected peaks for brg-H. Then the depleted brg-H site allows more brf site to adsorb H, causing the second brf-H peak to overlap with the first brf-H peak. After the brf sites are all occupied, the brg sites are occupied again as U goes below 0.25 V, which gives a flat peak just below the combined brf-H peak. As U decreases further, the tcn and fcc sites get occupied along with the remaining brg sites, contributing to the peak at ~ 0 V.

For H-adsorption on alloyed PdPt NPs, besides six different sites, occupations are also associated to the underneath alloy configurations, which may change with different H-coverages. The origin of the peaks in CV for alloyed PdPt NPs can be traced to those from pure Pd and Pt NPs. For brf-H on $Pd_{36}Pt_{19}$ (Fig. 5(c)), there exist one peak at ~0.35V for brf-H on Pt site (brf-H-Pt) and two broader peaks at 0.15 and −0.15 V due to brf-H-Pd; and the features in between are given by brf-H on other alloy configurations . With increasing $c_{Pt}$, the two brf-H-Pd peaks will gradually diminish and their contributions shift towards higher U, combining to a broader and more significant brf-H-Pt peak at 0.35V. The deviation of brg-H peaks from Pd toward Pt is also evident and the negative/depletion peak for brg-H just starts to appear. The position of the fcc-H peak (0.08 V) for $Pd_{36}Pt_{19}$ lies in between that of pure Pd (0.12 V) and Pt (−0.02 V), an

indication that the fcc-H adsorption strength decreases continuously as $c_{Pt}$ increases. On the

other hand, the tcn-H peak (−0.05 V) has already shifted much closer to the corresponding tcn-H

peak for Pt (~ 0V), far away from that of Pd (~ −0.6 V). The tsq-H peak is shifted to even more

negative U and ted-H peak has a splitting to ted-H-Pd (−0.8 V) and ted-H-Pt (−0.5 V). These

features are all from the interplay of multi-site adsorption and have their origins in the optimal

set of ECIs.

To better show the result, we plot the CV in 2D color contours spanned by both U and $c_{Pt}$ in

Fig. 5(d). The alloying effect on H-adsorption isotherm is not and should not be linear. At high-

U range, the H-brf-Pt peak at 0.35 V is already established at $c_{Pt} = 0.3$. In contrast, the peak at 0

V having contributions from brg, fcc and tcn sites only emerges as a single peak for $c_{Pt} > 0.6$. At

low-U range, the ted-H peak at ~ −0.8 V first shifts toward lower U for $c_{Pt} < 0.2$, then shift back

and split into two for $0.3 < c_{Pt} < 0.5$ and changes to a narrow peak at ~ −0.4 V for $0.6 < c_{Pt} <$

0.9. Our 2D CV with alloying effect on adsorption isotherm fully included allows one to inspect

the evolution of CV peaks as a function of nanoalloy composition and provides insights in

understanding the interplay of the multi-site adsorption contributions.

The H-adsorption isotherm $\theta(U, c_{Pt})$ is also plotted in Fig.5(e) to show the gradual increase of

H-coverage as U is swept to negative. The places with a color/gradient change correspond well

to the peak positions in Fig. 5(d) as their derivatives.

To show the correlation between H-adsorption isotherm and NP alloying configurations, we

plot in Fig. 5(f) the shell concentration of Pt, $c_{Pt}^{shell}$, for core-shell reversal behavior. Clearly, the

2D map is divided by the 50-50 boundary into two regions. In the Pd-rich (Pt-rich) region on the

bottom (top), the shell is always Pd-rich (Pt-rich). The core-shell reversal is bounded by the

range of $c_{Pt} = 0.4$-$0.6$, a NP geometric size effect.[10] Besides the main step-like feature for the core-shell reversal as H-coverage increases when U is swept to negative, there are more details for Pd-Pt-H than the strong core-shell reversal in PdRh-O. These details correlate well with the H-adsorption isotherm in Fig. 5(e) and in turn with the CV in Fig. 5(d). For example, for the NP at $c_{Pt} = 0.6$, as the H-coverage increases when U swept to lower value, $c_{Pt}^{shell}$ first increases toward U=0 V, next decreases and then increases again, which is closely correlated with the different H-adsorption peaks in Fig. 5(d).

Lastly, our new hybrid-ensemble MC simulation method based on the non-exchangeable coupled-lattice CE is not restricted to a 55-atom cuboctahedral NP. Future studies are planned on the effects of alloyed NP shape and size on the adsorption isotherm for detailed comparison to experiments.

**Conclusions.** To include NP alloying effect on adsorption isotherm to simulate cyclic voltammetry (CV) in electrocatalysis, we proposed and applied a hybrid-ensemble Monte Carlo (MC) simulation using the non-exchangeable coupled-lattice cluster expansion (CE) formalism extended for nanoalloys with adsorbates. In this scheme, adsorbates take MC steps in grand canonical ensemble and NP alloys take MC steps in canonical ensemble, which describes fully the alloying effect on CV (through the DFT-derived CE interactions fitted at the selected adsorbate coverages). For the hydrogen evolution reaction (HER) on Pd-Pt nanoalloys, we simulated the H-adsorption isotherm to calculate CV, and detailed the correlated configurational thermodynamics of nanoalloys with H-adsorption. Due to the coupling of comparable metal-metal, metal-H, and H-H interactions, the evolution of features in the adsorption isotherm and CV versus nanoalloy composition is highly non-linear and reflects the interplay among the multi-

site adsorption that closely correlates to alloy configurations. This new hybrid-ensemble MC directly predicts adsorption isotherms and CV for nanoalloys with adsorbates and will permit computationally-guided design of nanoalloy catalysts under electrochemical conditions.

## ACKNOWLEDGEMENTS

## AUTHOR INFORMATION

E-mail: *llw@ameslab.gov, § ddj@ameslab.gov

### Notes
The authors declare no competing financial interest.

## References

(1)      Ferrando, R.; Jellinek, J.; Johnston, R. L. **2008**, *108*, 845-910.

(2)      Tao, F.; Grass, M. E.; Zhang, Y.; Butcher, D. R.; Renzas, J. R.; Liu, Z.; Chung, J. Y.; Mun, B. S.; Salmeron, M.; Somorjai, G. A. *Science* **2008**, *322*, 932-934.

(3)      Tao, F.; Grass, M. E.; Zhang, Y.; Butcher, D. R.; Aksoy, F.; Aloni, S.; Altoe, V.; Alayoglu, S.; Renzas, J. R.; Tsung, C.-K.; Zhu, Z.; Liu, Z.; Salmeron, M.; Somorjai, G. A. *J. Am. Chem. Soc.* **2010**, *132*, 8697-8703.

(4)      Renzas, J. R.; Huang, W. Y.; Zhang, Y. W.; Grass, M. E.; Hoang, D. T.; Alayoglu, S.; Butcher, D. R.; Tao, F.; Liu, Z.; Somorjai, G. A. *Phys. Chem. Chem. Phys.* **2011**, *13*, 2556-2562.

(5)      Xin, H. L. L.; Alayoglu, S.; Tao, R. Z.; Genc, A.; Wang, C. M.; Kovarik, L.; Stach, E. A.; Wang, L. W.; Salmeron, M.; Somorjai, G. A.; Zheng, H. M. *Nano Lett.* **2014**, *14*, 3203-3207.

(6)      Besenbacher, F.; Chorkendorff, I.; Clausen, B. S.; Hammer, B.; Molenbroek, A. M.; Nørskov, J. K.; Stensgaard, I. *Science* **1998**, *279*, 1913-1915.

(7)      Kyriakou, G.; Boucher, M. B.; Jewell, A. D.; Lewis, E. A.; Lawton, T. J.; Baber, A. E.; Tierney, H. L.; Flytzani-Stephanopoulos, M.; Sykes, E. C. H. *Science* **2012**, *335*, 1209-1212.

(8)      Maroun, F.; Ozanam, F.; Magnussen, O. M.; Behm, R. J. *Science* **2001**, *293*, 1811-1814.

(9)      Shan, S. Y.; Petkov, V.; Yang, L. F.; Luo, J.; Joseph, P.; Mayzel, D.; Prasai, B.; Wang, L. Y.; Engelhard, M.; Zhong, C. J. *J. Am. Chem. Soc.* **2014**, *136*, 7140-7151.

(10)     Wang, L. L.; Tan, T. L.; Johnson, D. D. *Nano Lett* **2014**, *14*, 7077-7084.

(11)     Sanchez, J. M.; Ducastelle, F.; Gratias, D. *Physica A* **1984**, *128*, 334-350.

(12)     Hohenberg, P.; Kohn, W. *Phys. Rev.* **1964**, *136*, B864-B871.

(13)     Kohn, W.; Sham, L. J. *Phys. Rev.* **1965**, *140*, A1133-A1138.

(14)     Sanchez, J. M.; Stark, J. P.; Moruzzi, V. L. *Phys. Rev. B* **1991**, *44*, 5411-5418.

(15)     Asta, M.; Wolverton, C.; de Fontaine, D.; Dreyssé, H. *Phys. Rev. B* **1991**, *44*, 4907-4913.

(16)     Wolverton, C.; Asta, M.; Dreyssé, H.; de Fontaine, D. *Phys. Rev. B* **1991**, *44*, 4914-4924.

(17)     Sluiter, M. H. F.; Watanabe, Y.; Fontaine, D. d.; Kawazoe, Y. *Phys. Rev. B* **1996**, *53*, 6137-6151.

(18)     van de Walle, A.; Ceder, G. *J. Phase Equilib.* **2002**, *23*, 348-359.

(19)     Zarkevich, N. A.; Johnson, D. D. *Phys. Rev. Lett.* **2004**, *92*, 255702.

(20)     Blum, V.; Hart, G. L. W.; Walorski, M. J.; Zunger, A. *Phys. Rev. B* **2005**, *72*, 165113.

(21)     Hart, G. L. W.; Blum, V.; Walorski, M. J.; Zunger, A. *Nat. Mater.* **2005**, *4*, 391-394.

(22)     Zarkevich, N. A.; Tan, T. L.; Johnson, D. D. *Phys. Rev. B* **2007**, *75*, 104203.

(23)     Zarkevich, N. A.; Tan, T. L.; Wang, L. L.; Johnson, D. D. *Phys. Rev. B* **2008**, *77*, 144208.

(24)     Abrikosov, I. A.; Ruban, A. V.; Skriver, H. L.; Johansson, B. **1994**, *50*, 2039.

(25)     Drautz, R.; Reichert, H.; Fähnle, M.; Dosch, H.; Sanchez, J. M. **2001**, *87*, 236102.

(26)    Chepulskii, R. V.; Butler, W. H.; van de Walle, A.; Curtarolo, S. *Scr. Mater.* **2010**, *62*, 179-182.

(27)    Wang, L.-L.; Tan, T. L.; Johnson, D. D. *Phys. Rev. B* **2012**, *86*, 035438.

(28)    Tan, T. L.; Wang, L.-L.; Johnson, D. D.; Bai, K. *Nano Lett.* **2012**, *12*, 4875-4880.

(29)    Yuge, K. *J. Phys.: Condens. Matter* **2010**, *22*, 245401.

(30)    Yuge, K. *Phys. Rev. B* **2011**, *84*, 085451.

(31)    Mueller, T. *Phys. Rev. B* **2012**, *86*, 144201.

(32)    Wang, L.-L.; Johnson, D. D. *J. Am. Chem. Soc.* **2009**, *131*, 14023-14029.

(33)    Tepesch, P. D.; Garbulsky, G. D.; Ceder, G. *Phys. Rev. Lett.* **1995**, *74*, 2272-2275.

(34)    Karlberg, G. S.; Jaramillo, T. F.; Skulason, E.; Rossmeisl, J.; Bligaard, T.; Norskov, J. K. *Phys Rev Lett* **2007**, *99*, 126101.

(35)    Tan, T. L.; Wang, L. L.; Johnson, D. D.; Bai, K. W. *J. Phys. Chem. C* **2013**, *117*, 22696-22704.

(36)    Tan, T. L.; Wang, L. L.; Zhang, J.; Johnson, D. D.; Bai, K. W. *ACS Catalysis* **2015**, *submitted*.

(37)    Liu, Y.; Chi, M. F.; Mazumder, V.; More, K. L.; Soled, S.; Henao, J. D.; Sun, S. H. *Chem Mater* **2011**, *23*, 4199-4203.

(38)    Lim, B.; Jiang, M. J.; Camargo, P. H. C.; Cho, E. C.; Tao, J.; Lu, X. M.; Zhu, Y. M.; Xia, Y. N. *Science* **2009**, *324*, 1302-1305.

(39)    Baranova, E. A.; Miles, N.; Mercier, P. H. J.; Le Page, Y.; Patarachao, B. *Electrochim Acta* **2010**, *55*, 8182-8188.

(40)    Adams, B. D.; Ostrom, C. K.; Chen, A. C. *J Electrochem Soc* **2011**, *158*, B434-B439.

(41)    Schmidt, D. J.; Chen, W.; Wolverton, C.; Schneider, W. F. **2011**, *8*, 264-273.

(42)    Nørskov, J. K.; Bligaard, T.; Logadottir, A.; Kitchin, J. R.; Chen, J. G.; Pandelov, S.; Stimming, U. **2005**, *152*, J23-J26.

(43)    Müller, S. **2003**, *15*, R1429.

(44)    Connolly, J. W. D.; Williams, A. R. *Phys. Rev. B* **1983**, *27*, 5169-5172.

(45)    Han, B. C.; Van der Ven, A.; Ceder, G.; Hwang, B.-J. *Phys. Rev. B* **2005**, *72*, 205409.

(46)    Kerscher, T. C.; Landgraf, W.; Podloucky, R.; Muller, S. *Phys. Rev. B* **2012**, *86*, 195420.

(47)    Wang, L.-L.; Khare, S. V.; Chirita, V.; Johnson, D. D.; Rockett, A. A.; Frenkel, A. I.; Mack, N. H.; Nuzzo, R. G. **2005**, *128*, 131-142.

(48)    Wang, L.-L.; Johnson, D. D. *J. Am. Chem. Soc.* **2007**, *129*, 3658-3664.

(49)    Hammer, B.; Hansen, L. B.; Norskov, J. K. *Phys Rev B* **1999**, *59*, 7413-7421.

(50)    Kresse, G.; Furthmuller, J. *Phys. Rev. B* **1996**, *54*, 11169-11186.

(51)    Kresse, G.; Furthmuller, J. *Comput. Mater. Sci.* **1996**, *6*, 15-50.